Electronic structures of [110]-faceted self-assembled pyramidal InAs/GaAs quantum dots

Lin-Wang Wang, Jeongnim Kim, and Alex Zunger
National Renewable Energy Laboratory, Golden, Colorado 80401
(Received 27 July 1998)

We calculate the electronic structures of pyramidal quantum dots with supercells containing 250 000 atoms, using spin-orbit-coupled, nonlocal, empirical pseudopotentials. We compare the results with previous theoretical calculations. Our calculation circumvents the approximations underlying the conventional effective-mass approach: we describe the potential, the strain and the wave functions using atomistic rather than continuum models. The potential is given by a superposition of screened atomic pseudopotentials, the strain is obtained from minimizing the atomistic strain energy, and the wave function is expanded using a plane-wave basis set. We find the following. (1) The conduction bands are formed essentially from single envelope functions, so they can be classified according to the nodal structure as s, p, and d. However, due to strong multiband coupling, most notably light hole with heavy hole, the valence states cannot be classified in the language of single-band envelope functions. In fact, the hole states have no nodal planes. (2) There is a strong anisotropy in the polarization of the lowest valence state to conduction state optical transition. This is in contrast to the eight band $\mathbf{k}\cdot\mathbf{p}$ model, which finds essentially zero anisotropy. (3) There are at least four bound electron states for a 113-Å-based quantum dot. This number of bound states is larger than that found in eight band $\mathbf{k}\cdot\mathbf{p}$ calculations. (4) Since our atomistic description retains the correct C_{2v} symmetry of a square-based pyramid made of zinc-blende solids, we find that the otherwise degenerate p states are split by about 25 meV. This splitting is underestimated in the eight-band $\mathbf{k}\cdot\mathbf{p}$ calculation. [S0163-1829(99)00608-6]

I. INTRODUCTION

Nanometer-sized semiconductor quantum dots can be grown in the Stranski-Krastanow mode using molecular beam epitaxy[1] or metal-organic chemical vapor deposition.[2] These growth techniques afford different sizes and shapes of InAs quantum dots grown on top of a GaAs substrate, once a critical layer thickness ($\sim$1.7 ML) of InAs has been deposited. The driving force for the formation of such quantum dots is the elastic energy associated with the InAs/GaAs lattice mismatch.[3] The potential applications of such quantum dot systems range from high yield lasers to single-electron devices.[4,5]

A few spectroscopic techniques have been applied to study the electronic structures of such InAs/GaAs quantum dots. These include photoluminescence (showing quantum confinement effects[6]), infrared absorption (showing conduction-band splittings[7]), capacitance measurements and charged exciton absorption (demonstrating electron-electron interaction and state filling[8]), and high-resolution single-exciton and multiexciton spectroscopy of isolated dots.[9–11]

Theoretical studies of such quantum dots are complicated by the facts that (i) their shapes are nontrivial (they are often faceted); (ii) they are subjected to *inhomogeneous* strain; (iii) they exhibit wave-function localization, implying strong multiband coupling; and (iv) single-particle energy spacings are comparable to the electron-hole Coulomb interactions. Theoretical investigations of such quantum dots have so far been based on the effective-mass approximation, ranging from single-band models (amenable to analytic solutions[12–14]), to few-band models.[15–18] These models are distinguished primarily by their varying abilities to handle different shapes and strain profiles, and by the number N of Brillouin-zone-center Bloch functions of the underlying bulk solid that are used to expand the states of the quantum dots. The sophistication of current theoretical methods increases from one-band effective mass[12–15] to an $N=4$ band $\mathbf{k}\cdot\mathbf{p}$ model,[16] to an $N=8$ band $\mathbf{k}\cdot\mathbf{p}$ model,[17–19] and finally to the pseudopotential method.[20] There are a number of reasons suggesting that $\mathbf{k}\cdot\mathbf{p}$ approaches may be insufficient for embedded quantum dots.

(i) *Wave-function localizations in a segment of the dot*: As was demonstrated recently by Pryor[18] and by Jiang and Singh,[17] the eight-band $\mathbf{k}\cdot\mathbf{p}$ model gives quite different results from the simpler (lower N) models. However, in the case of free-standing quantum dots,[21,22] it has been shown that even the 6–8 band $\mathbf{k}\cdot\mathbf{p}$ model are still insufficient to describe the extensive interband coupling. On the one hand, the size of the embedded quantum dots is usually a few times larger than that of the free-standing (colloidal) quantum dots (InP or CdSe). Thus, one might think that the eight-band $\mathbf{k}\cdot\mathbf{p}$ model will be more applicable here than in the case of free-standing quantum dots. On the other hand, however, due to the inhomogeneous strain present in embedded dots, the wave functions are often localized in a small segment of the quantum dot;[20] thus the limiting physical dimension of the wave function might still be similar to that of free-standing quantum dots.

(ii) *The continuum treatment of interfaces*: When quantum dots become small, the atomic nature of the interfaces, neglected by continuum approaches, may become important. For example, the conventional $\mathbf{k}\cdot\mathbf{p}$ model[15,17–19] treats an unstrained, square-based, pyramidal quantum dot as having C_{4v} symmetry. In reality, the system has only C_{2v} symmetry since the atomic structure is different in the [110] and [1$\bar{1}$0] directions.

(iii) *Retention of only the linear effects of strain on the*

electronic states (Ref. 18): The adequacy of this linear approximation has not been tested in the case of InAs/GaAs, where large (7%) strains exist.

(iv) *The neglect or the simplification of the electron-hole Coulomb interaction*: As shown recently,[23] the calculation of Coulomb energies from envelope functions, rather than from microscopic wave functions of the quantum dots overestimates the Coulomb energy by as much as 40%.

Points (i)–(iv) above suggest that it might be desirable to calculate the electronic structure of quantum dots using a method which has fewer approximations than the conventional $\mathbf{k}\cdot\mathbf{p}$ model. Here we offer a treatment that avoids approximations (i)–(iv).

In this paper, we study the electronic structure of InAs/GaAs quantum dots using our newly developed atomistic pseudopotential method.[5] This approach describes the potential, the strain, and the wave functions using *atomistic*, rather than continuum models. The potential is given by a superposition of screened atomic pseudopotentials, the strain is calculated from minimizing the atomistic strain energy, and the wave functions are not restricted to envelope functions but retain the microscopic part. Consequently, multiband coupling is not limited, atomic features in the density are resolvable, and the deformation potentials are not linearized, thus avoiding the approximations underlying the $\mathbf{k}\cdot\mathbf{p}$ calculations. The approximations that are involved include lack of charge self-consistency and a phenomenological treatment of the size- and position-dependent dielectric screening. The same approach has achieved very good agreement with experiment for free-standing quantum dots, including band gap vs size for Si,[24] InP,[25] and CdSe,[26] high-energy excitonic spectra of InP (Ref. 27) and CdSe,[22] pressure effects on InP,[28] and exchange splitting in InP (Ref. 29) and CdSe.[5,30] This approach has also been applied to study embedded nanostructures, including pressure effects on InAs/GaAs quantum dots[31] and a GaAs/AlAs ''Russian doll.''[32] Here we report atomistic calculations (including the spin-orbit interaction) for large embedded dots (containing a 250 000 atoms in the supercell). This is made possible by the development of a parallel computer code on the Cray T3E computer. Here we present the results of this calculation for an InAs/GaAs pyramidal quantum dot, analyzing the electron and hole wave functions in real space, and calculating the polarizations of the interband optical transitions and the size dependence of the confined energy levels. We compare our results with the previous $\mathbf{k}\cdot\mathbf{p}$ calculations.

II. METHODS OF CALCULATIONS

A. Shape and strain

Despite a few years of experimental studies, the shape of Stranski-Krastanow ''self-assembled'' quantum dots is still controversial. Indeed, various shapes have been proposed for InAs/GaAs quantum dots, including [110]-faceted square-based pyramids,[33] lens shape,[34] flat oblate pancake shape,[35] and [136]-faceted pyramid.[36] Since the main purpose of this study is to compare the present approach to other theoretical methods, and since others have chosen to study mostly [110]-faceted square-based pyramidal quantum dots,[15–18,33,37] we will do the same here. In another paper,[20] we studied the effects of various shapes on the electronic structures of the quantum dots (but without including the spin-orbit interactions).

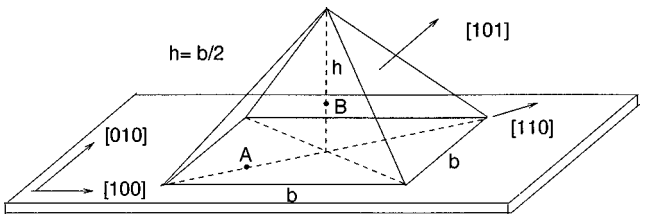

FIG. 1. Schematic view of the pyramidal quantum dot. The InAs quantum dot is buried in the GaAs matrix. The wetting layer is one monolayer thick. The base length b of the pyramid equals $n\times a$, where a is the zinc-blende lattice constant. We have calculated four systems with b equal to $20a, 18a, 16a$ and $12a$. The points A and B are used in Figure 5.

Figure 1 provides a schematic view of the square pyramid with [101], $[\bar{1}01]$, and [011] facets. Although, in a rigid-body description, a square-based pyramid implies C_{4v} symmetry,[15,16] the actual symmetry of the pyramid (made of zinc-blende crystal) is[38] C_{2v}. This is because at the atomistic level, the [110] and $[\bar{1}10]$ directions are not equivalent

We place an As atom at the origin (0,0,0) of the coordinate system and a Ga atom at the $(\frac{1}{4},\frac{1}{4},\frac{1}{4})a$ position (where a is the zinc-blende lattice constant). In our notation, the pyramid's tip points to the positive z direction. Our [110] direction is thus defined as the line pointing from the (0,0,0) site to the (1,1,0) site. Considering the bottom interface between the InAs pyramid and the GaAs substrate, this is the direction of the As-In-As-In atomic chain on the InAs side of the interface. Note that others, e.g., Lee and co-workers,[19] used different convention by placing Ga atom at (0,0,0) and As at $(\frac{1}{4},\frac{1}{4},\frac{1}{4})a$. Thus their $[\bar{1}10]$ direction is equivalent to our [110] direction.

We calculate the electronic structure of four quantum dots with bases sizes b equal to $12a$, $16a$, $18a$, and $20a$, respectively, where $a=5.6533$ Å is the lattice constant of bulk zinc-blende GaAs. We model the wetting layer using a monolayer-thick InAs layer at the base of the pyramid (Fig. 1). To calculate the strain and the electronic structure, we place the InAs pyramid and its wetting layer in a large box, filled with GaAs, and repeat this ''supercell'' periodically, to create a mathematically convenient periodicity. Once the geometry of the pyramid is so determined, the atomic displacements due to the InAs/GaAs lattice mismatch are calculated by minimizing the strain energy using Keating's atomistic valence-force-field (VFF) (Refs. 39 and 40) model. The VFF potential and the parameters we used are the same as in Ref. 17, and are also described in Ref. 38. To relax the atomic positions, we use a $40a\times 40a\times 50a$ periodic supercell. Such a large supercell is needed to reduce the unphysical elastic dot-dot interaction, so its effect in the electronic energy level is less than 3 meV. The resulting strain profiles for such pyramidal dots are reported in Ref. 38. Comparison with the continuum elasticity model shows that the atomistic calculation gives an anisotropic strain profile along [110] and $[\bar{1}10]$ directions. The difference with regard to the continuum model is particularly large near the InAs/GaAs interface.

TABLE I. The pseudopotential parameters (in atomic units). See Eqs. (2)–(4) for the definitions.

	a_0	a_1	a_2	a_3	γ_α	β_α
Ga	6.155×10^4	2.270	3.210×10^3	0.6248	1.6295	-0.010
In	101.3	1.883	5.052	0.4881	1.336	-0.037
As (in GaAs)	6.15	2.884	1.151	0.2606	0.0	-0.010
As (in InAs)	46.53	2.620	1.972	0.6931	0.0	-0.010

Since the electronic states are confined mostly inside the dots, a smaller supercell is adequate for a description of the wave functions. Indeed, the dot-dot interaction due to wavefunction overlap is much smaller than the long-range dot-dot interaction due to elastic strain. Consequently, for the purpose of calculating the wave functions, we have removed a few GaAs layers from the original $40a\times40a\times50a$ supercell, reducing it to a $28a\times28a\times30a$ supercell. The atomic positions of the atoms inside and near the pyramid are kept the same as in the original $40a\times40a\times50a$ supercell. The atoms in the periphery layers of the $28a\times28a\times30a$ box have been relaxed again, so that a smooth, periodic boundary condition can be formed. The single-particle electronic levels calculated (by the method to be described below) using this reduced supercell differ by less than 0.1 meV from those obtained using the original $40a\times40a\times50a$ supercell, although the saving in computational effort is substantial. We emphasize that the shapes of the dot and wetting layer are ''inputs'' to the calculation, and any choice can be entertained.

B. Electronic structure calculations

Having formulated the atomic structures of the dot, wetting layer, and barrier, the electronic structure is obtained next using a direct-diagonalization approach to the single-particle Schrödinger equation in a pseudopotential representation,

$$\left\{-\frac{1}{2}\nabla^2+\sum_{n\alpha}\hat{v}_\alpha(\mathbf{r}-\mathbf{R}_{n\alpha})\right\}\psi_i(\mathbf{r})=\epsilon_i\psi_i(\mathbf{r}). \tag{1}$$

Due to the spin-orbit coupling, the wave function $\psi_i(\mathbf{r})$ is complex and has both spin-up and spin-down components. $\mathbf{R}_{n\alpha}$ denotes the positions of the nth atom of type α, determined from the strain minimization described in Sec. II A above. $\hat{v}_\alpha(\mathbf{r}-\mathbf{R}_{\mathbf{n}\alpha})$ is the screened pseudopotential[41] of atom type α. It contains a local part and a nonlocal spin-orbit interaction part.

Since our calculation is non-self-consistent, we have to construct screened potentials that emulate as much as possible the effects of self-consistency. This is done in two ways. First, the potential for the common anion (As) is allowed to differ slightly, depending on if its nearest-neighbors are Ga or In (Table I). Second, we introduce in the potential $\hat{v}^{\rm loc}_\alpha(\mathbf{r}-\mathbf{R}_{\mathbf{n}\alpha})$ a dependence on the *local* atomic environment, e.g., the hydrostatic strain $\mathrm{Tr}(\boldsymbol{\epsilon})$ of the atoms at $\mathbf{R}_{\mathbf{n}\alpha}$,

$$v^{\rm loc}_\alpha(r;\boldsymbol{\epsilon})=v^{\rm eq}_\alpha(r;0)[1+\gamma_\alpha\,\mathrm{Tr}(\boldsymbol{\epsilon})], \tag{2}$$

where γ_α is a fitting parameter. The zero strain potential $v^{\rm eq}_\alpha(r;0)$ is expressed in reciprocal space q as

$$v(q)=a_0(q^2-a_1)/[a_2e^{a_3q^2}-1]. \tag{3}$$

The local hydrostatic strain $\mathrm{Tr}(\boldsymbol{\epsilon})$ for a given atom at $\mathbf{R}$ is defined as Ω_R/Ω_0-1, where Ω_R is the volume of the tetrahedron formed by the four atoms bonded to the atom at $\mathbf{R}$. Ω_0 is the volume of that tetrahedron in the unstrained condition (bulk InAs or GaAs). The explicit dependence of the pseudopotential on strain is a feature necessitated by the requirement to fit the local density approximation (LDA)-derived self-consistent absolute deformation potential of the valence band.[41] In the absence of this term, one obtains an incorrect sign (positive, instead of negative) for the deformation potential of the valence band.

The nonlocal spin-orbit interaction $\hat{v}^{\rm nonloc}_\alpha$ in $\hat{v}_\alpha(\mathbf{r}-\mathbf{R}_{\mathbf{n}\alpha})$ is described by a Kleinmen-Bylander separable form[42]

$$\hat{v}^{\rm nonloc}_\alpha=\beta_\alpha\sum_{i,j}|i\rangle B(i,j)\langle j|, \tag{4}$$

where $|i\rangle$ and $|j\rangle$ are reference functions, and $B(i,j)$ is a matrix representation of the spin-orbit interaction: $B(i,j)=\langle i|\mathbf{L}\cdot\mathbf{S}|j\rangle$, where $\mathbf{L}$ and $\mathbf{S}$ are the spatial angular momentum operator and spin operator, respectively. We only considered the spin-orbit coupling between p-like states. Thus there are six reference states $|i\rangle$ $(=|p_x^\uparrow\rangle,\ |p_y^\uparrow\rangle,\ |p_z^\uparrow\rangle,\ |p_x^\downarrow\rangle,\ |p_y^\downarrow\rangle$, and $|p_z^\downarrow\rangle)$. Each state $|i\rangle$ is normalized. Details of the implementation of Eq. (4) are given in Ref. 43.

The pseudopotential of Eqs. (2)–(4) is fitted to the measured bulk band structures, hydrostatic and biaxial deformation potentials, and spin-orbit splittings.[41] Where direct experimental data are not available, we have used LDA calculated results. These include the band offset between InAs and GaAs (at the InAs and at the GaAs lattice constants), and the absolute deformation potentials of the valence bands. The pseudopotential parameters used are listed in Table I. Some of the bulk band structure properties obtained with this potential are listed in Table II.

The wave function ψ_i in Eq. (1) (complex, having a spin-up and a spin-down components) is expanded by plane waves. An energy cutoff of 5 Ry is used to select the plane-wave basis.[44] This cutoff suffices, since it was designed at the outset in the fitting process of the pseudopotential. Fast Fourier transforms are used to transform the wave function back and forth between a real space grid and a reciprocal space grid. A $16\times16\times16$ real space grid is used for each eight-atom zinc-blende cubic cell. Equation (1) is solved by

TABLE II. Properties of the InAs and GaAs pseudopotential band structures at their respective nature lattice constants of 6.0583 and 5.6533 Å . E_g is the band gap, while $E_{\rm vbm}$ is the VBM energy relative to the vaccum level. Δ_0 is the spin-orbit splitting, and $a_g(\Gamma)$, $a_c(\Gamma)$, and $a_v(\Gamma)$ are the deformation potentials of the gap, the conduction-band minimum, and the valence-band maximum, respectively. b and d are the uniaxial and shear deformation potentials of the valence band. To calculate d, a shear strain with elongation along the $\langle 111\rangle$ direction is applied, and the internal atomic displacement is calculated using the VFF method.

	InAs	GaAs
E_g (eV)	0.404	1.518
$E_{\rm vbm}$ (eV)	-5.570	-5.622
$E_{X_{1c}}-E_{\rm vbm}$ (eV)	2.270	1.949
$E_{L_{1c}}-E_{\rm vbm}$ (eV)	1.410	1.745
m_e	0.032	0.092
$m_{\rm hh}[100]$	0.48	0.47
$m_{\rm lh}[100]$	0.040	0.122
Δ_0 (eV)	0.35	0.33
$a_g(\Gamma)$ (eV)	-5.34	-8.63
$a_c(\Gamma)$ (eV)	-6.19	-9.63
$a_v(\Gamma)$ (eV)	-0.85	-1.00
b (eV)	-1.85	-1.77
d (eV)	-3.32	-3.1

the folded spectrum method,[45] which solves for only a few states near the valence-band maximum (VBM) and conduction-band minimum (CBM). The computational time of the folded spectrum method scales linearly with the number of atoms. Using a parallelized code on a Cray T3E machine, we are able to calculate a 250 000 atom system within 10 cpu hours on 128 nodes.

III. RESULTS

A. Confined electron and hole levels

We have calculated four conduction states and four valence states for each quantum dot. The four conduction state energies for the pyramid with a base size of $b=20a$ are -4.4230, -4.3305, -4.3068, and -4.2483 eV (measured from the vacuum level), and are labeled from CBM to CBM+3, respectively. The four hole-state energies for the same system are at -5.3823, -5.3926, -5.4027, and -5.4094 eV and are labeled from VBM to VBM-3, respectively. In Fig. 2 , we show the quantum size dependence of the electron and hole energy levels. The energies are compared with the CBM and VBM of the monolayer-thick wetting layer, which are calculated separately in a coherently strained quantum-well geometry with atomic positions calculated from the VFF model. From Fig. 2 we see that there are at least four bound-electron states for the $b=20a$ system, consistent with our previous, non-spin-orbit interaction calculations.[20] The four calculated hole states are well above the VBM of the wetting layer. As the dot size is reduced, the valence-band energies become more negative while the conduction band energies become less negative. As expected, quantum confinement thus causes the number of bound-electron states to decrease as the size of the quantum dot is reduced. As we can see, the number of bound-electron state is reduced to 2 for the $b=12a$ pyramid system.[46]

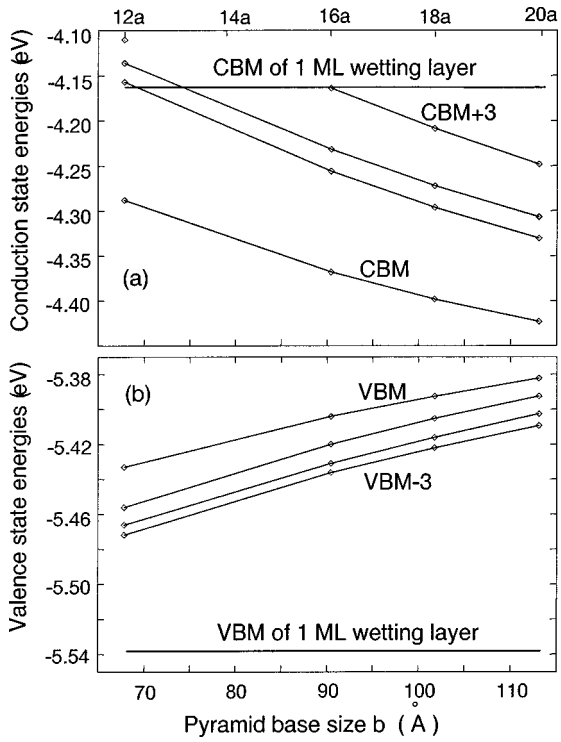

FIG. 2. The conduction- and valence-band bound-state energies as functions of the pyramid base length b ($=n\times a=n\times 5.6533$ Å). The horizontal lines represent the CBM and VBM energy of the 1-ML wetting layer.

B. Confined wave functions

In Fig. 3 we show the isosurface plots of the conduction- and valence-band wave-function amplitude $|\psi_i(\mathbf{r})|^2$ for the $b=20a$ pyramidal dots, while Fig. 4 shows similar results for $b=12a$ dot. The blue and green isosurface levels are selected as 0.75 and 0.25 of the maximum wave-function amplitude, respectively.

For both pyramids, the lowest conduction state is an s-like state, while the next two conduction states CBM+1 and CBM+2 are p-like states localized along $[\bar{1}10]$ and $[110]$ directions, respectively. The s-p splitting $\Delta_{sp}=E_{\rm CBM+1}-E_{\rm CBM}$ is 93 meV for the $b=20a$ pyramid. The energies of the p-like CBM+1 and CBM+2 states are different due to the existence of C_{2v}, rather than C_{4v} symmetry. This is true even in the absence of strain. Strain further splits these states (since the strain profile along $[110]$ and $[\bar{1}10]$ are unequal.[38]) We find a p-state splitting $\Delta_{pp}=E_{\rm CBM+2}-E_{\rm CBM+1}$ of about 25 meV, almost independent of the quantum dot size (Fig. 2). On the other hand, $\mathbf{k}\cdot\mathbf{p}$ models, using continuum elasticity to describe strain[15], or neglecting strain,[13,14] assume a C_{4v} symmetry, so they predict a degeneracy of such levels ($\Delta_{pp}=0$) for a square-based pyramid. To split these states, such models need to distort the shape of the square-based pyramid[19] to, e.g., a rhombohedral base. The piezoelectric effect can also split these two states. But, according to the

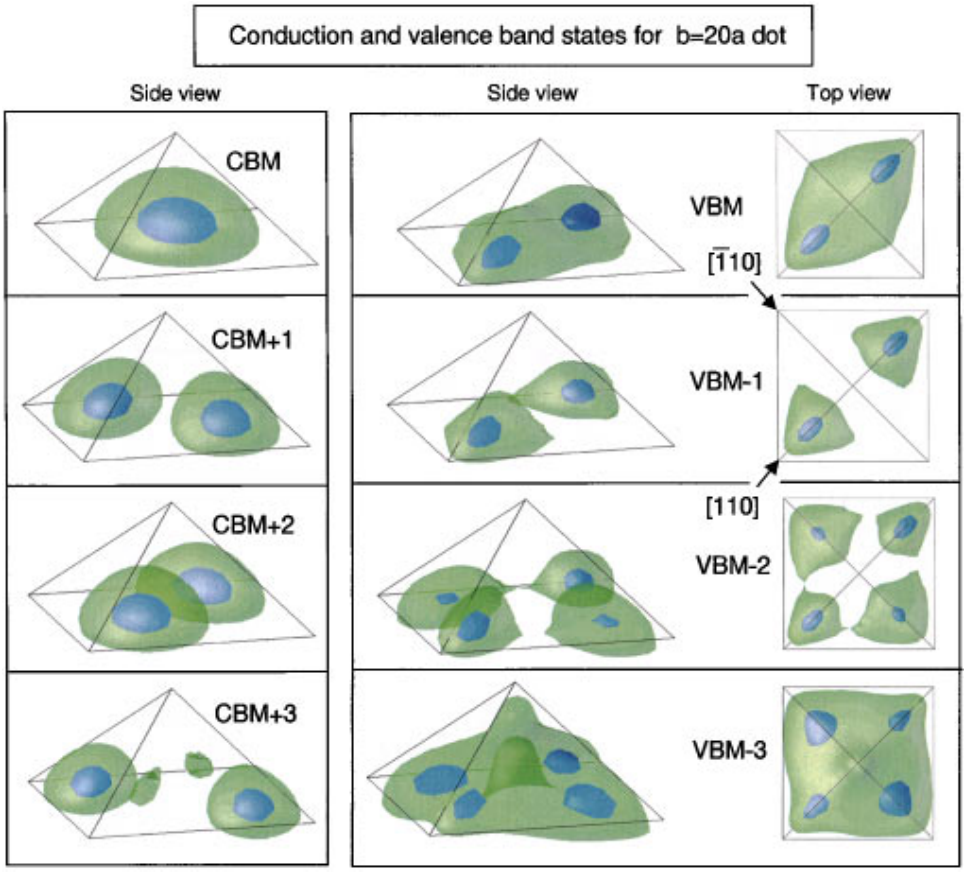

FIG. 3. (Color) Isosurface plots of the charge densities of the conduction- and valence-band states for the $b=20a$ pyramids. The charge density equals the wave-function square, including the spin-up and -down components. The level values of the green and blue isosurfaces equal 0.25 and 0.75 of the maximum charge density, respectively.

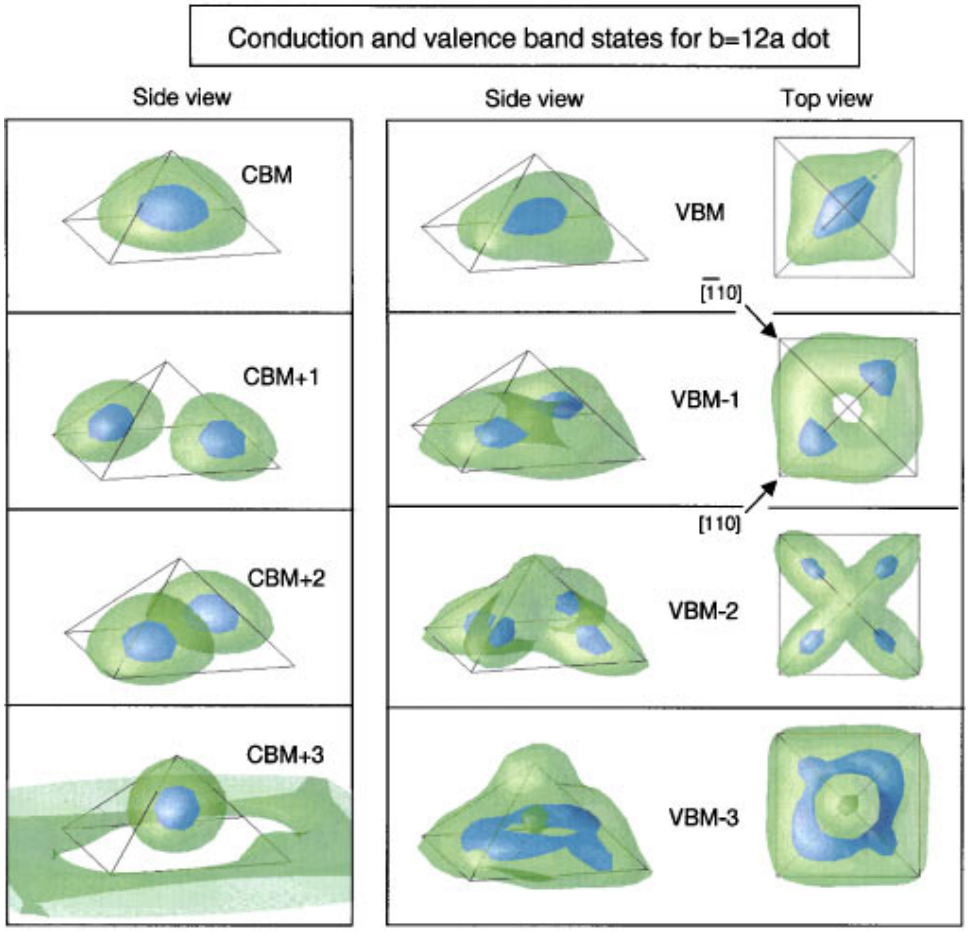

FIG. 4. (Color) Isosurface plots of the charge densities of conduction- and valence-band states for the $b=12a$ pyramids. See the caption of Fig. 3 for more details.

recent eight-band $\mathbf{k}\cdot\mathbf{p}$ calculation by Pryor,[18] the piezoelectric effect only splits the two *p*-like states by 2 meV for the $b=20a$ quantum dot. This is ten times smaller than the splitting caused by the anisotropy of the atomic structure. Thus the piezoelectric effect can be safely neglected.

The CBM+3 conduction state in the $b=20a$ dot is *d* like, with two nodal planes along the [110] direction. This is also true for the CBM+3 state in the $b=16a$ and the $18a$ based dots. However, for the $b=12a$ dot, the CBM+3 state is resonant with a wetting layer state, so the wave function leaks into the wetting layer.

In a previous study,[20] we showed the isosurface plots for conduction states and valence states calculated without the spin-orbit interactions. As expected, the current calculation (which includes the spin-orbit interaction) yields almost the same results for the conduction states, but different results for the valence states. For example, the VBM calculated with spin-orbit interaction has fewer structures than its counterpart in the non-spin-orbit interaction calculation. Note that, although the corresponding isosurfaces of the valence states of the $b=20a$ and $b=12a$ quantum dots look different, they are actually qualitatively the same state with the same polarization properties.[47] Thus, as the size of the pyramid changes, there is no valence-band state crossing.

An interesting result obtained from our atomistic calculation is that while the conduction states of the dot are made essentially of single-envelope functions, and so can be classified as being *s* like (CBM), *p* like (CBM+1 and CBM +2), *d* like (CBM+3), etc., the valence states represent such a strong band mixing that they cannot be classified according to their nodal structure as being *s* like, *p* like, etc. *In fact, our calculated valence state of Figs. 3 and 4 show no nodal planes.*[47] We conclude that the valence states cannot be classified according to their nodal structures being *s* like, *p* like, etc. The approximation[15,48] of using a single heavy-hole band to describe the valence state is thus qualitatively incorrect. This is because, unlike the case of one dimensional quantum well or superlattice, in dots the heavy hole and light hole are mixed very strongly so as to be inseparable.

C. Electron-hole Coulomb energies

The Coulomb interaction between the valence states and the conduction states is calculated as

$$J_{i,j}=\int\int \frac{|\psi_{i,v}(\mathbf{r}_1)|^2|\psi_{j,c}(\mathbf{r}_2)|^2}{\bar{\epsilon}(\mathbf{r}_1-\mathbf{r}_2)|\mathbf{r}_1-\mathbf{r}_2|}d^3\mathbf{r}_1 d^3\mathbf{r}_2, \qquad (5)$$

where $|\psi|^2$ includes the sum of spin-up and spin-down components. $\bar{\epsilon}(\mathbf{r}_1-\mathbf{r}_2)$ is a distant dependent dielectric function consisting of an electronic part and an ionic part. The details of this function have been described elsewhere.[22,30] Here, in Eq. (5) we use the dielectric function $\bar{\epsilon}(\mathbf{r}_1-\mathbf{r}_2)$ of bulk InAs. The interaction $J_{i,j}$ between the valence and conduction states are listed in Table III for the $b=20a$ pyramid. The values of $J_{\mathrm{vbm,cbm}}$ for the $b=12a$, $16a$, $18a$, and $20a$ pyramids are 42.5, 34.2, 30.8, and 27.7 meV, respectively. These values are slightly larger than the eight-band $\mathbf{k}\cdot\mathbf{p}$ results reported by Pryor,[18] bearing in mind that a dielectric constant (instead of a function of $|\mathbf{r}_1-\mathbf{r}_2|$) is used there. Notice that the Coulomb interaction energies are of similar magnitudes as the single-particle splittings among the valence bands (Fig. 2). Thus these Coulomb energies are important to explain the spectroscopic fine structures, especially when multiexcitons are involved.[10]

TABLE III. The Coulomb interaction energy $J_{i,j}$ [Eq. (5)] between the valence states and conduction states, for the $b=20a$ pyramid. The numbers are in meV units.

	CBM	CBM+1	CBM+2	CBM+3
VBM	27.7	24.4	27.2	22.8
VBM-1	24.3	22.1	25.9	21.3
VBM-2	23.5	23.7	23.0	22.9
VBM-3	25.7	24.8	24.3	23.5

D. Polarizations and dipole matrix elements of interband transitions

The valence (v) to conduction (c) interband optical transition matrix elements $|\langle\psi_{i,v}|\mathbf{p}|\psi_{j,c}\rangle|^2$ and their polarization directions are given in Table IV for the $b=20a$ quantum dot. None of the calculated transitions have a ''pure polarization direction'' (we define ''pure polarization direction'' as the direction along which the optical transition is not zero, while transitions along orthogonal directions have zero amplitudes). Nevertheless, there are some preferred polarization directions. In Table IV, we list the polarization directions corresponding to the strongest transition amplitudes. Table IV shows that the VBM to CBM transition is allowed for

TABLE IV. First line: the transition matrix elements $\Sigma_{i,j}|\langle\psi_{v_i}|\mathbf{p}|\psi_{c_j}\rangle|^2/2$, summed over the Kramer's doublet for each valence- and conduction-band state. The numbers shown here are in atomic units and pertain to the $b=20a$ quantum dot. Second line: the major polarization directions. We use the notations $u_+=[110]$, $u_-=[\bar{1}10]$, and $z=[001]$. The first polarization given corresponds to the strongest transition amplitude. Only the polarizations which have transition amplitudes larger than one-fifth of the first polarization are listed. Third line: the amplitude ratio $u_+/u_-/z$.

	CBM	CBM+1	CBM+2	CBM+3
VBM	0.1475	0.0045	0.0046	0.0073
	u_+, u_-	z,u_-	z,u_-	u_+, u_-
	1/0.8/0.001			
VBM-1	0.0006	0.0336	0.1049	0.0036
	z,u_-	u_-,u_+	u_+, u_-	z,u_-,u_+
			1/0.6/0.009	
VBM-2	0.0146	0.0013	0.0002	0.0684
	u_-	z,u_-	u_-,u_+	u_+, u_-
				1/1.0/0.0005
VBM-3	0.0215	0.0867	0.0160	0.0014
	z,u_-,u_+	u_+, u_-	u_+, u_-	u_-,u_+
		1/0.9/0.01		

both [110] and $[\bar{1}10]$ polarizations, but forbidden for z polarization, while the transitions to the second and third (p-like) conduction bands are allowed in z polarization. The transition from the second valence band to the CBM is rather weak, and is z polarized. Table IV shows the following. (i) All valence-to-conduction transitions are allowed. (ii) The strongest transition occurs along the $[110] \equiv u_+$ and $[\bar{1}10] \equiv u_-$ directions. (iii) There are significant polarization anisotropies between u_+ and u_- directions. Defining the intensity ratio along the two substrate directions as

$$\frac{I_{ij}[110]}{I_{ij}[\bar{1}10]} = \frac{|\langle \psi_{i,v}|P_{[110]}|\psi_{j,c}\rangle|^2}{|\langle \psi_{i,v}|P_{[\bar{1}10]}|\psi_{j,c}\rangle|^2} \tag{6}$$

we have, for the VBM to CBM transitions,

$$\frac{I_{ij}[110]}{I_{ij}[\bar{1}10]} = \begin{cases} 1.35, & \text{Expt. Ref. 19,} \\ 1.26, & \text{Square-based pyramid: present calc.} \\ 0.97, & \text{Square-based pyramid: } \mathbf{k}\cdot\mathbf{p}+\text{VFF calc. Ref. 19,} \\ 1.80, & [136]-\text{shaped-dot; } \mathbf{k}\cdot\mathbf{p}+\text{VFF calc. Ref. 19.} \end{cases} \tag{7}$$

We see that the present atomistic calculation predicts a significant polarization anisotropy even for a square-based pyramid, while a continuum, eight-band $\mathbf{k}\cdot\mathbf{p}$ calculation predicts for the same structure a polarization ratio of 0.97 (if the strain is calculated[19] atomistically via the VFF model) or 1 (if the strain is modeled via continuum elasticity). This is because effective mass based methods do not capture the correct physical symmetry, e.g., they incorrectly view the square-based pyramid as having the same symmetry along [110] and $[\bar{1}10]$. To obtain a polarization ratio larger than 1, the $\mathbf{k}\cdot\mathbf{p}$ model needs to distort the pyramid, e.g., to the [136] rhombohedral shape[19] (note that the present definitions of the [110] and $[\bar{1}10]$ directions are the reverse of that used in Ref. 19, while Eq. (7) uses a consistent set of definition). We see that, based on the current calculation, the major part of the experimental anisotropy can already be explained by a square-based pyramidal quantum dot. While we are not ar-

TABLE V. Summary of the assumptions (''input'') and main results (''output'') of various theoretical calculations for the InAs/GaAs quantum dot. Under ''shape'' we recognize the square-based [110]-faceted pyramid (P) as P[110]. Under ''strain'' we denote calculations using a continuum elasticity description as ''CE,'' and those using atomistic, valence-force-field, strain as ''VFF.'' ''Strain anisotropy'' means whether or not the model distinguishes strain along [110] and $[\bar{1}10]$. ''Number of bands'' refers to the number of Bloch states used to expand the dot states. m_e and m_{hh} are electron and heavy hole effective masses. $E_{\rm cbo}$ and $E_{\rm vbo}$, respectively, are ''natural'' (unstrained) conduction- and valence-band offsets: $E_{\rm cbo}=E_{\rm CBM}$(InAs) $-E_{\rm CBM}$(GaAs) and $E_{\rm vbo}=E_{\rm VBM}$(InAs) $-E_{\rm VBM}$(GaAs). In the present calculation, they are determined from accurate LDA results (Ref. 51). a_c and a_v are the conduction- and valence-band-edge absolute deformation potentials. The values used here are from accurate LDA calculations (Refs. 49 and 50). In the ''output'' section, $N^e_{\rm bound}$ are the number of bound electron states (excluding spin degeneracy). The s-p splitting in the conduction band is $\Delta_{sp}=E_{\rm CBM+1}-E_{\rm CBM}$. The splitting of the upper two valence-band states is $\Delta_{\rm vb}=E_{\rm VBM}-E_{\rm VBM-1}$. The single-particle band gap (without Coulomb correction) is E_g. The quantum dot calculated in Ref. 13, is not pure InAs, but an $In_{0.5}Ga_{0.5}As$ alloy. The results listed are for a quantum dot with a base diameter (or the size of the square) equal to 113 Å.

	Ref. 13	Ref. 14	Ref. 15	Ref. 16	Ref. 17	Ref. 18	Current
Shape	Lens	Cone	P[110]	P[110]	P[110]	P[110]	P[110]
Strain	None	None	CE	CE	VFF	CE	VFF
Strain anisotropy	None	None	None	None	Yes	None	Yes
No. of bands	1	1	1	4	8	8	Many
m_e (InAs)	0.067	0.067	0.023	0.04	0.022	0.022	0.032
$m_{\rm hh}^{[001]}$(InAs)		0.34	0.034	0.34	0.34	0.34	0.48
$E_{\rm cbo}$ (eV)	-0.35	-1.167	-1.085	-1.085	-1.085	-1.015	-1.062
$E_{\rm vbo}$ (eV)		0.053	0.025	0.025	0.025	0.085	0.052
a_c(InAs) (eV)			-5.08	-5.08	-5.08	-6.66	-6.19
a_v(InAs) (eV)			1.00	1.00	1.00	0.66	-0.85
$N^e_{\rm bound}$	1	1	1	1	3	3	$\geqslant 4$
Δ_{sp} (meV)	100	100	–	150	88	97	93
$\Delta_{\rm vb}$ (meV)			77	17	14	25	10
E_g (eV)		1.4	1.09	1.17	1.01	1.20	0.96

guing that the experimental shape is a square-based pyramid, this calculation does demonstrate that the measured polarization ratio cannot, by itself, determine the shape. This comparison further highlights the importance of *atomistic* calculations when quantitative comparisons are needed between experiment and theory.

E. Comparison with other calculations

As mentioned in Sec. I, one of the purposes of the current study is to compare the current pseudopotential calculations with previous calculations for similar systems. In Table V, we list some important ''input parameters,'' and the results for some of the previous calculations for the InAs/GaAs quantum dots. As we can see, in addition to differences in the assumed quantum dot shapes and number of Bloch bands used in the basis and treatment of strain, different research groups have also used different parameters for the values of the effective masses, deformation potentials, and band offsets. Our absolute deformation potentials a_v and a_c, as well as the band offsets, are obtained from accurate LDA calculations.[49,50] Note that while the energy of bulk Γ_{1c} conduction band goes up as the material is compressed ($a_c<0$ in Table V), most groups have assumed that the energy of the bulk valence band maximum goes down ($a_v>0$ in Table V). Accurate LDA calculations[50] show that this is not the case.

For a similar-sized quantum dot, our calculation predicts the largest number N^e_{bound} of bound-electron states and the smallest valence-band splitting $\Delta_{\text{vb}}=E_{\text{VBM}}-E_{\text{VBM}-1}$. The electronic Hamiltonian used in the literature ranges from the one-band effective mass, to the four-band $\mathbf{k}\cdot\mathbf{p}$ approximation, to the eight-band $\mathbf{k}\cdot\mathbf{p}$ approximations, and to the current many-band coupled pseudopotential representation. The comparisons between one-band, four-band, and eight-band $\mathbf{k}\cdot\mathbf{p}$ results were carried out by Pryor.[18] His main result was that, compared to the 1–4-band $\mathbf{k}\cdot\mathbf{p}$ models, the eight-band $\mathbf{k}\cdot\mathbf{p}$ model predicts smaller quantum confinement effects (smaller E_g), and thus a larger number of bound states N^e_{bound}. From Table V, we see that the same trend continues from the eight-band $\mathbf{k}\cdot\mathbf{p}$ calculation to the current pseudopotential calculation. The number of bound-electron states increases from $N^e_{\text{bound}}=3$ in the eight-band $\mathbf{k}\cdot\mathbf{p}$ calculation to $N^e_{\text{bound}}\geqslant 4$ in the pseudopotential calculations. While the *s*-*p* splitting we find between the CBM and CBM+1 is similar to that obtained in previous calculations, the splitting Δ_{vb} we find between the VBM and VBM−1 is much smaller than the results of previous calculations. While Pryor[18] used continuum elasticity to calculate the atomic relaxations, and thus found no *p*-state splitting between CBM+1 and CBM+2 states, Jiang and Singh[17] used the same VFF model and parameters as in the present study. So, at least, the strain-induced portion of the CBM+1 and CBM+2 splitting is included in their calculation. This *p*-state splitting in their eight-band $\mathbf{k}\cdot\mathbf{p}$ calculation is about 10 meV (Fig. 3 of Ref. 17), which is a factor of 2 smaller than our 24-meV result. Note that, even if there is no strain anisotropy (for example, when all atoms are fixed at the ideal GaAs lattice positions), our pseudopotential model still produces a *p*-state splitting and polarization anisotropy due to the atomistic difference at the interface, while the eight-band $\mathbf{k}\cdot\mathbf{p}$ model will not produce such splitting and anisotropy.

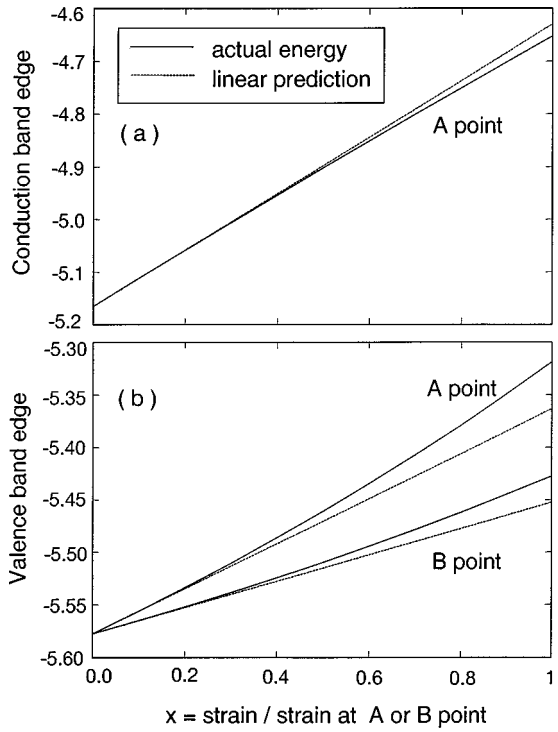

FIG. 5. The energy of the conduction-band edge (a) and valence-band edge (b) for different strains. The strain is normalized to its value at points *A* and *B* shown in Fig. 1 for the $b=20a$ pyramid. The solid lines show the changes of energies of bulk CBM and VBM as obtained by the pseudopotential method. The strain changes from that in natural bulk InAs ($x=0$), to the actual strain at the *A* and *B* points ($x=1$). The dashed lines show the predictions obtained using linear deformation potentials.

More complicated and interesting than the conduction-band states are the valence-band states. As discussed above, our valence state cannot be described by single-band envelope function as suggested in Ref. 33. Unfortunately, we cannot make a direct comparison with the eight-band $\mathbf{k}\cdot\mathbf{p}$ results, since detailed descriptions of the valence states are not given in Ref. 18 and 17. However, the polarizations we obtain are different from the results in Ref. 17. This is an indication that our valence states are different from those of Ref. 17. Furthermore, our energy vs size curve in Fig. 2(b) does not resemble its counterpart in Fig. 4 of Ref. 18 (for example, we do not have state crossing at $b\sim 105$ Å). This is another indication that the pseudopotential and the eight-band $\mathbf{k}\cdot\mathbf{p}$ models might not have the same valence states or valence state order.

The importance of strain effects on the band structure was emphasized by Pryor.[18] Here, we point out that, not only the linear part (deformation potential), but also the nonlinear part of the strain effect are important for accurate calculations. In Fig. 5 we show the dependence of the valence- and conduction-band energy on the ratio between the actual strain and the maximum strains (taken from points *A* and *B* in the pyramid, as shown in Fig. 1). We can see that if only the linear deformation potential is used (dashed lines in Fig. 5), a $\sim$50 meV error might result. This not a small error, since the order of the valence state is often determined by a

~10-meV energy difference. These nonlinear strain effects are not represented in the current eight-band $\mathbf{k}\cdot\mathbf{p}$ models.[13–15,17–19] In our pseudopotential model, we have taken into account the nonlinear effects by fitting to the LDA band structures at a few different strains relevant to the pyramidal quantum dot. Since our pseudopotential of Eq. (3) is close to the *ab initio* potential, it represents the nonlinear effects in an intrinsic way.[44,41]

IV. SUMMARY

We have used the pseudopotential approach, including spin-orbit interactions, to calculate the electronic structure of square-based pyramidal quantum dots. We find the following. (1) While the conduction bands are essentially derived from well-defined single-envelope functions, the valence states show massive interband coupling. As a result, the valence states have no nodal planes and therefore cannot be classified as s, p, and d states. As a consequence, the optical spectrum of such dots cannot be interpreted using simplified descriptions (successful in quantum wells) that include only heavy-hole states or only light-hole states. Another consequence of the strong coupling between hole states is that the lowest interband transition has a very different intensity along each of the two in-plane substrate directions [110] and $[\bar{1}10]$. This anisotropy exists even in the absence of strain (thus reflecting pure band coupling) and is absent in typical $\mathbf{k}\cdot\mathbf{p}$ calculations. (2) There are $\geqslant 4$ bound electron states for the $b=20a$ pyramidal quantum dot. This number is larger than that obtained in the $\mathbf{k}\cdot\mathbf{p}$ model, and consistent with the current experimental results. The energy splitting between the p-like conduction bands found in the present study is a factor of 2 larger than the $\mathbf{k}\cdot\mathbf{p}$ results. (3) The current method and the $\mathbf{k}\cdot\mathbf{p}$ method appear to have different valence states or different orders of the valence states.

ACKNOWLEDGMENTS

The authors would like to thank A. J. Williamson for useful discussions, and a careful reading of the manuscript. This work was supported by the U.S. Department of Energy–Basic Energy Science, Division of Materials Science, under Contract No. DE-AC36-83CH10093. The computational aids were provided by the National Energy Research Scientific Computer Center (NERSC).

[1] B. G. Levi, Phys. Today **49** (6), 22 (1996).
[2] W. Seifert *et al.*, Prog. Cryst. Growth Charact. Mater. **33**, 423 (1996).
[3] B. J. Spencer and J. Tersoff, Phys. Rev. Lett. **79**, 4858 (1997).
[4] P. L. McEuen, Science **278**, 1729 (1997); and other quantum dot articles in the same issue.
[5] *Semiconductor Quantum Dots*, edited by Alex Zunger, special issue of MRS Bull **23**, No. 2 (1998).
[6] A. Forchel, R. Steffen, T. Koch, M. Michel, M. Albrecht, and T. L. Reinecke, Semicond. Sci. Technol. **11**, 1529 (1996).
[7] M. Fricke, A. Lorke, J. P. Kotthaus, G. Medeiros-Ribeiro, and P. M. Petroff, Europhys. Lett. **36**, 197 (1996).
[8] R. J. Warburton, C. S. Durr, K. Karrai, J. P. Kotthaus, G. Medeiros-Ribeiro, and P. M. Petroff, Phys. Rev. Lett. **79**, 5282 (1997).
[9] L. Landin, M. S. Miller, M.-E. Pistol, C. E. Pryor, and L. Samuelson, Science **280**, 262 (1998).
[10] E. Dekel, D. Gershoni, E. Ehrenfreund, D. Spektor, J. M. Garcia, and P. M. Petroff, Phys. Rev. Lett. **80**, 4991 (1998).
[11] T. Saiki, K. Nishi, and M. Ohtsu, Jpn. J. Appl. Phys. **37**, 1638 (1998).
[12] A. Barenco and M. A. Dupertuis, Phys. Rev. B **52**, 2766 (1995).
[13] A. Wojs, P. Hawrylak, S. Fafard, and L. Jacak, Phys. Rev. B **54**, 5604 (1996).
[14] J.-Y. Marzin and G. Bastard, Solid State Commun. **92**, 437 (1994); Ph. Lelong and G. Bastard, *ibid.* **98**, 819 (1996).
[15] M. Grundmann, O. Stier, and D. Bimberg, Phys. Rev. B **52**, 11 969 (1995).
[16] M. A. Cusack, P. R. Briddon, and M. Jaros, Phys. Rev. B **54**, R2300 (1996).
[17] H. Jiang and J. Singh, Phys. Rev. B **56**, 4696 (1997).
[18] C. Pryor, Phys. Rev. B **57**, 7190 (1998).
[19] W. Yang, H. Lee, and P. C. Sercel (unpublished); H. Lee, W. Yang, R. Lowe-Webb, and P. C. Sercel (unpublished); P. C. Sercel (private communication).
[20] J. Kim, L. W. Wang, and A. Zunger, Phys. Rev. B **57**, R9408 (1998).
[21] H. Fu, L. W. Wang, and A. Zunger, Phys. Rev. B **57**, 9971 (1998).
[22] L. W. Wang and A. Zunger, Phys. Chem. Miner. **102**, 6449 (1998).
[23] A. Franceschetti and A. Zunger, Phys. Rev. Lett. **78**, 915 (1997).
[24] L. W. Wang and A. Zunger, in *Semiconductor Nanoclusters*, edited by P. V. Kamat and D. Meisel (Elsevier, Amsterdam, 1996).
[25] H. Fu and A. Zunger, Phys. Rev. B **56**, 1496 (1997).
[26] L. W. Wang and A. Zunger, Phys. Rev. B **53**, 9579 (1996).
[27] H. Fu and A. Zunger, Phys. Rev. B **57**, R15 064 (1998).
[28] H. Fu and A. Zunger, Phys. Rev. Lett. **80**, 5397 (1998).
[29] O. I. Micic, H. M. Cheong, H. Fu, A. Zunger, J. R. Sprague, A. Mascarenhas, and A. J. Nozik, J. Phys. Chem. B **101**, 4904 (1997).
[30] A. Franceschetti, L. W. Wang, H. Fu, and A. Zunger, Phys. Rev. B (to be published).
[31] A. J. Williamson and A. Zunger, Phys. Rev. B **58**, 6724 (1998).
[32] J. Kim, L. W. Wang, and A. Zunger, Phys. Rev. B **56**, R15 541 (1997).
[33] M. Grundmann *et al.*, Phys. Status Solidi **188**, 249 (1995); S. Ruvimov, P. Werner, K. Scheerschmidt, U. Gösele, J. Heydenreich, U. Richter, N. N. Ledentsov, M. Grundmann, D. Bimberg, V. M. Ustinov, and A. Yu. Egorov, Phys. Rev. B **51**, 14 766 (1995).
[34] D. Leonard, M. Krishnamurthy, C. M. Reaves, S. P. Denbaars, and P. M. Petroff, Appl. Phys. Lett. **63**, 3203 (1993); D. Leonard, K. Pond, and P. M. Petroff, Phys. Rev. B **50**, 11 687 (1994).
[35] Q. Xie *et al.*, J. Cryst. Growth **150**, 357 (1995); G. S. Solomon, M. C. Larson, and J. S. Harris, Appl. Phys. Lett. **69**, 1897 (1996).

[36] H. Lee, R. Lowe-Webb, W. Yang, and P. C. Sercel, Appl. Phys. Lett. **72**, 812 (1998).

[37] M. Grundmann, J. Christen, N. N. Ledentsov, J. Böhrer, D. Bimberg, S. S. Ruvimov, P. Werner, U. Richter, U. Gösele, J. Heydenreich, V. M. Ustinov, A. Yu. Egorov, A. E. Zhukov, P. S. Kop'ev, and Zh. I. Alferov, Phys. Rev. Lett. **74**, 4043 (1995).

[38] C. Pryor, J. Kim, L. W. Wang, A. J. Williamson, and A. Zunger, J. Appl. Phys. **83**, 2548 (1998).

[39] P. Keating, Phys. Rev. **145**, 637 (1966).

[40] R. Martin, Phys. Rev. B **1**, 4005 (1970).

[41] A. J. Williamson, J. Kim, L. W. Wang, S. H. Wei, and A. Zunger (unpublished).

[42] L. Kleinman and D. M. Bylander, Phys. Rev. Lett. **48**, 1425 (1982).

[43] Equation (4) is implemented in real space, on a fast Fourier transform grid of the wave function ψ_i. The $|p_x\rangle$, $|p_y\rangle$, and $|p_z\rangle$ reference functions are approximated by x, y, and z times a spherical Bessel function $j_1(4.493r/r_{cut})$, which has its first node at $r=r_{cut}$. The reference functions outside r_{cut} are set to zero. We have used $r_{cut}=2.25$ a.u for all In, Ga, and As atoms, deduced from the size ranges of the spin-orbit interaction nonlocal pseudopotentials in the local density approximation.

[44] A smooth energy cutoff (with a smooth cutoff parameter of 0.8) is used in the current calculation, and is defined in L. W. Wang and A. Zunger, Phys. Rev. B **51**, 17 398 (1995).

[45] L. W. Wang and A. Zunger, J. Chem. Phys. **100**, 2394 (1994).

[46] According to Fig. 2, the third electron state in the $b=12a$ dot is above the wetting layer CBM energy. However, as shown in Fig. 4, this state is a normal p-like bound state. This contradiction might result from the finite supercell we used, which has limited wetting layer area, thus pushes the wetting layer CBM energy up. So, in reality, according to Fig. 2, the $b=12a$ quantum dot should have only two bound electron states.

[47] Consider the VBM-1 state in Figs. 3 and 4. If we lower the isosurface value from 0.25 to 0.1, the two lumps of the green isosurfaces of the $b=20a$ dot in Figs. 3 will be connected to form a doughnut, similar to the isosurface plot of VBM-1 state of the $b=12a$ quantum dot shown in Figs. 4. Similarly, the VBM-2 and VBM-3 states change from the $b=20a$ plots in Fig. 3 to $b=12a$-like plots in Fig. 4, when the isosurface value changes from 0.25 to 0.1. Thus the wave-function square of the valence state does not have any nodal plane.

[48] M. Grundmann, N. N. Ledentsov, O. Stier, J. Bohrer, and D. Bimberg, Phys. Rev. B **53**, R10 509 (1996).

[49] A. Franceschetti, S. H. Wei, and A. Zunger, Phys. Rev. B **50**, 17 797 (1994).

[50] S.H. Wei (unpublished).

[51] S. H. Wei and A. Zunger, Appl. Phys. Lett. **72**, 2011 (1998).